Asian Journal of Chemistry; Vol. 35, No. 12 (2023), 2971-2978

ASIAN JOURNAL OF CHEMISTRY

https://doi.org/10.14233/ajchem.2023.30294

Facile Synthesis of Core-Shell Nanoparticles Silver/Cr_2O_3 Embedded with Ultrathin MoS_2 Layers, Microstructure Analysis and Biocompatibility Enhancement by *in vitro* Evaluation of Antiproliferation and Antibacterial Activities

M. Lakshmidevi, L. Suresh, S. Prabu, E. Bhakya Lakshmi, P. Vasanthi, E. Kala and M. Kayalvizhi*

Department of Chemistry, Kalaignar Karunanidhi Government Arts College, Tiruvannamalai-606603, India

*Corresponding author: E-mail: kayalpappa78@gmail.com

Received: 14 September 2023; *Accepted*: 19 October 2023; *Published online*: 2 December 2023; AJC-21457

Cost-effective methods were employed in this study to synthesize core-shell nanoparticles of silver/Cr_2O_3 (SM) embedded with ultrathin MoS_2 layers (SM1) to increase the properties and biocompatibility of the nanomaterials. For structural and morphological investigation, powder XRD, TEM, SEM, EDAX and XPS were used. Magnetic behaviour of SM and SM1 nanoparticles investigated by VSM was shown to be ferromagnetic, and when MoS_2 nanosheets were injected, their magnetism decreased. The zeta potential of SM1 was also analyzed. This nanomaterial was synthesized to test the biocompatibility effectiveness of anticancer and antibacterial compounds. In MCF-7 adenocarcinoma (breast cancer) and HepG-2 hepatocellular carcinoma (liver cancer) cell lines, SM1 was investigated for antiproliferation effectiveness. The MCF-7 and HepG-2 cell lines both showed strong cytotoxic potential. Antimicrobial activity was observed against *Staphylococcus aureus* and *Escherichia coli*. This study provides strong evidence to support the development of cytotoxicity and antimicrobial properties for significant biomedical compatibility by demonstrating a key to understanding the Ag/Cr_2O_3 nanoparticle embedded in 2D MoS_2 nanosheets on forming a unique interaction as well as the strategy for achieving *in vitro* efficiency.

Keywords: Nanocomposite, Ferromagnetic, Transition metal dichalcogenides, SOD, Oxidative stress, Anti-proliferation.

INTRODUCTION

Nanobiomaterials development and applications in biomedicine open up new pathways for disease diagnosis and treatment [1-3]. Several researchers have been working on synthesizing and studying nanomaterials with adjustable properties, good targeting ability, low toxicity and various capabilities for various biomedical applications [4]. Because of their many redox states, antioxidant activity and biocompatibility, nano-metal oxides with dichalcogenides have recently gained much interest. Chromium oxide nanocomposite has been focused on vital attention due to its versatile properties and applications, essential as a heterogeneous catalyst, pigment, solar energy collector, *etc*. [5-7]. It is mainly used as a catalyst in many organic reactions, such as oxidation, due to its high band gap of ~ 3 eV. Because of its high band gap energy, Cr_2O_3 nanocomposites enhance their properties depending on the type of material combined with that composite. The properties of Cr_2O_3 were less studied and very sensitive depending on the combination and reaction [8].

Several transition metal chalcogenide are decorated by noble metals (Au, Ag, Pd, Pt) owing to their high activity and non-structural damage to the original species [9]. Within the category of noble metals, silver stands out as the most cost-effective and highly conductive metal. Incorporating silver into decorative elements does not significantly impact the overall material expense. It can be used as an ideal substituent in biological applications. Because of this, Ag-doped Cr_2O_3 has recently drawn attention to enhance the properties of Cr_2O_3 nanoparticles.

Ultrathin MoS_2 layers have achieved much attention in recent years form transition metal dichalcogenides family for its diverse applications in photodetectors, batteries and optoelectronics [10-12]. With the swift development of ultrathin layered MoS_2 deposited on the catalyst's surface as a co-catalyst to transfer photogenerated electrons [13-15]. Molybdenum disulfide (MoS_2) exhibits resistance to the influence of oxygen and dilute acids, and demonstrates semiconducting characteristics as a result of its band gap of 1.23 eV. The MoS_2 nanosheet is a repre-

sentative example of a 2D semiconductor and a graphene analogue. It is formed by the arrangement of S-Mo-S units, which are covalently bonded and held together by weak van der Waals forces [16].

MoS_2 nanosheets exhibit unique physical, optical and electrical properties correlated with their 2D ultrathin atomic layer structure and high surface area [17-19]. The supporting substrates sometimes offer synergistic effects to the intrinsic properties of the nanoparticles, making the composites much more attractive in applications in various materials than the nanoparticles alone. The monolayer of MoS_2 has found several uses in fields such as field-effect transistors, photodetectors, solar cells, chemical sensors, supercapacitor electrodes and valleytronics devices [20].

In this study, $Ag/Cr_2O_3@MoS_2$ nanosheet layers were synthesized utilizing a low-cost thermal decomposition approach and functionalized with DMSA before being self-assembled with as-prepared MoS_2 nanosheets using ultrasonication. Their structural, morphological, compositional and magnetic characterization studies were presented, as well as *in vitro* studies of the potent proliferative activity assessment of MCF-7 and HepG-2 human cancer cells and antimicrobial activities to check the nanocomposite material's biological applicability.

EXPERIMENTAL

Synthesis of Ag/Cr_2O_3: Ag/Cr_2O_3 nanoparticles were prepared by sol-gel auto-combustion method. In this method, precursors silver chloride and chromium chloride hexahydrate were dissolved in water in stoichiometry ratio 1:2 with addition of urea and citric acid. Further the solution was heated with simultaneous stirring using a magnetic stirrer. The pH of the solution was maintained at 7. The solution was then allowed to air dry slowly with continuous stirring for 46 h to form the gel. On the following day, the same solution was vigorously stirred and the solvent evaporator was around 40 ºC. At 120 ºC, after almost all solvents had evaporated, urea began to breakdown, releasing NH_3. The decomposition of urea can be detected by the presence of NH_3 odour and the formation of bubbles within the mixture. Subsequently, a desiccated gel materialized and underwent heating at 250 ºC till the attainment of a dark green powder through combustion.

Functionalization of Ag/Cr_2O_3 nanoparticles: To prepare $Ag/Cr_2O_3/MoS_2$ core-shell particles, Ag/Cr_2O_3 has to be activated to trap with MoS_2. For this, to functionalize the SM nanoparticles, dimercaptosuccinic acid (DMSA) in deionized water at pH ~ 10 was added to SM nanoparticles (ratio 5:1), which were dispersed in THF and sonicated for 1 h and then stirred for 3 h. The solution was washed several times using deionized water and centrifuged the solution to remove excess DMSA and THF [21]. The precipitate was dispersed in deionized water for further use.

Synthesis of MoS_2 nanosheets: Synthesis of MoS_2 nanosheets was achieved by Morrison method [22]. In brief, 2 mg bulk MoS_2 powder was dissolved in 10 mL of *n*-butyl lithium in hexane under nitrogen atmosphere. After intercalation for 48 h, the mixture was washed thoroughly using hexane. The residue was dissolved in deionized water. With ultrasonication, the lithium atoms between the MoS_2 layers interacted with water and the generation of H_2 gas, pushing the nanosheets apart. By centrifuging this solution, multilayered MoS_2 nanosheets were obtained by removing the excess hexane and lithium ions and dispersing them in deionized water.

Synthesis of Ag/Cr_2O_3-MoS_2 (core-shell): To prepare $Ag/Cr_2O_3/MoS_2$ core-shell nanoparticles, by ultrasonicating the mixture of an aqueous solution of DMSA-modified SM nanoparticles by slow addition of an aqueous solution of multilayered MoS_2 nanosheets feeding mass ratio 1:5. Final product was precipitated by magnetic stirring for 12 h, the addition of saline and centrifugated the product from sonication. The precipitate is heated in an oven at 100 ºC for 24 h to get a dry SM1 sample for further analysis.

Characterization: The powder X-ray diffraction pattern of SM1 was recorded with the XPERT-PRO system with the copper anode ($K\alpha$ = 1.54060 Å) at 25 mA/40 kV with 1000 W of X-ray power. A Perkin-Elmer PHI-5300 Thermo-Scientific K-alpha XPS spectrometer was used to analyze the surface of the material. The magnetization of SM1 was examined using a vibrating sample magnetometer (VSM Model 7404, USA). The morphological nanomaterial was characterized using transmission electron microscopy (model: JEOL JEM 2010).

Cell lines: The cell lines MCF-7 and HepG-2 were obtained from the National Centre for Cell Sciences (NCCS), Pune, India. The cell lines were treated with 10% fetal bovine serum and incubated at 37 ºC with 5% CO_2.

MTT assay: The cell lines were cultured and incubated for 24 h in 96-well microtiter plates. At the suitable concentrations, the sample was introduced to the plate cells. After that, the cells were cultured for 24 h. Following the initial incubation time, addition of 10 mL of 3-(4,5-dimethylthiazol-2-yl)-2,5-diphenyltetrazolium bromide (MTT: 1 mg/mL) was done to each well. The plates were then incubated in a dark environment for 3 h at 37 ºC. By cleaving to a tetrazolium ring, succinate-dehydrogenase, a mitochondrial enzyme in living cells, converts MTT to insoluble formazan. As a result, the quantity of formazan produced is proportional to the number of viable cells [23]. Each sample was incubated for 24 h with 15 mL of MTT (5 mg/mL) in PBS (pH ~7.2). At five dilutions, the anticancer activity of the synthesized materials was assessed and the control cells were those that were not exposed to SM1. The % cell inhibition growth concentration of the samples was estimated.

Antibacterial assay: The antibacterial activity of the synthesized nanomaterials was examined against Gram-positive *Staphylococcus aureus* and Gram-negative *Escherichia coli*. Before sub-culture, the cultures were placed in an agar plate and incubated at 35 ºC. A 100 µL of prepared bacterial inoculum was marked on the Mueller-Hinton agar surface using a swab to examine the antibacterial activity of nanoparticles in the disc diffusion method [11]. The impregnated discs with varying nanoparticle concentrations of 25, 50, 75 and 100 µg/mL were then placed on the surface of the injected agar plate in 50 µL DMSO as solvent. Finally, the plates were incubated for 24 h at 37 ºC.

RESULTS AND DISCUSSION

Powder XRD studies: Fig. 1 shows XRD diffraction pattern of the samples. The diffraction peaks corresponding to α-Cr_2O_3 are indexed and matched according to JCPDS card no. 38-1479 having rhombohedral phase $a = b = 4.953$ Å; $c = 13.578$ Å (Table-1). The significant peak at 38.16º is attributed to Ag (111) plane consistent with the face-centered cubic (fcc) structure of typical polycrystalline silver nanoparticles. Table-1 shows the prominent peaks of silver nanoparticles (JCPDS card no. 4-0783) [24]. Significantly less intense peaks (Table-1) of MoS_2 were observed due to the low concentration and ultra-thin thickness of MoS_2 nanoparticles (JCPDS card no. 65-0160) [25]. The peak broadening nature could be attributed to the nanosize of the sample, which is confirmed by Scherrer's formula and the average crystallite size is given in Table-1.

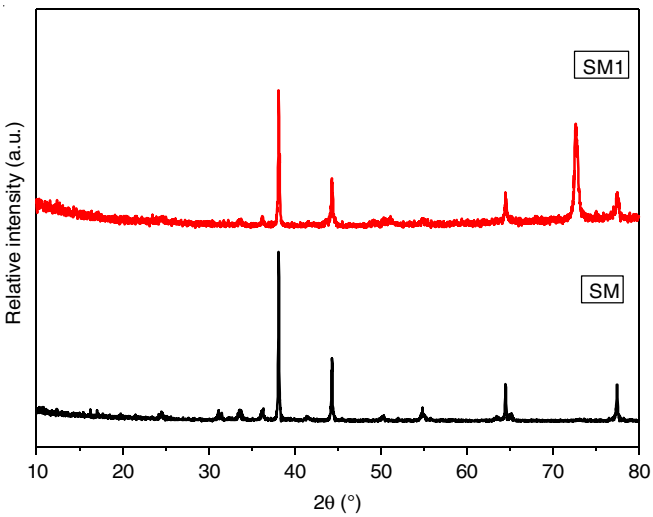

Fig. 1. Powder X-ray diffraction pattern of SM and SM1 nanocrystalline particles

The average crystallite size of the samples was calculated using Scherrer's formula:

$$D = \frac{k\lambda}{B_{(khl)} \cos\theta} \quad (1)$$

TABLE-1
PEAK POSITION AND hkl VALUES OF α-Cr_2O_3, Ag NANOPARTICLES AND MoS_2 ULTRATHIN LAYER

α-Cr_2O_3		Ag nanoparticles		MoS_2 ultrathin layer	
Peak position (2θ) (°)	*hkl*	Peak position (2θ) (°)	*hkl*	Peak position (2θ) (°)	*hkl*
24.48	012	38.1	111	14.39	200
33.60	104	44.3	200	29.02	004
36.24	110	64.4	220	35.88	100
39.70	006	77.3	311	36.68	102
41.52	113			39.55	103
44.40	202				
50.44	024				
54.91	116				
58.40	122				
63.45	214				
65.10	300				
72.90	101				
73.30	119				

Average crystallite size of SM and SM1 is 36 and 49 nm, respectively.

where D is the crystallite size (A), λ is the wavelength of the X-ray radiation (A), K is usually taken as 0.89, β is the line width at half-maximum height (radians) and θ is the diffraction angle (°).

TEM and SEAD studies: The nanoparticles diameter was observed from the TEM images (Fig. 2a-b) and the shell thickness was optimized to 40-45 nm. The average crystallite sizes of the samples SM and SM1 were found to be 36 and 49 nm, respectively, which are well-agreed with powder XRD data. Fig. 2b shows that the significant variation of shell thickness subsists between the particles and the thickness varies even within a single hollow silver/Cr_2O_3 nanoparticle. In addition, the particle deviates from the exact spherical shape for most of the particles.

It can be seen from the Fig. 2b that many ultrathin layers of MoS_2 were attached to Ag/Cr_2O_3 nanocomposite, which is considered to be ultrathin MoS_2 layers supported by powder XRD data. From the TEM images, it was confirmed that the coexistence of Ag, Cr_2O_3 and ultrathin MoS_2 was observed. Ag nanoparticles were predominantly spherical and visible of the hollow Ag nanoparticles embedded on Cr_2O_3 and an ultra-

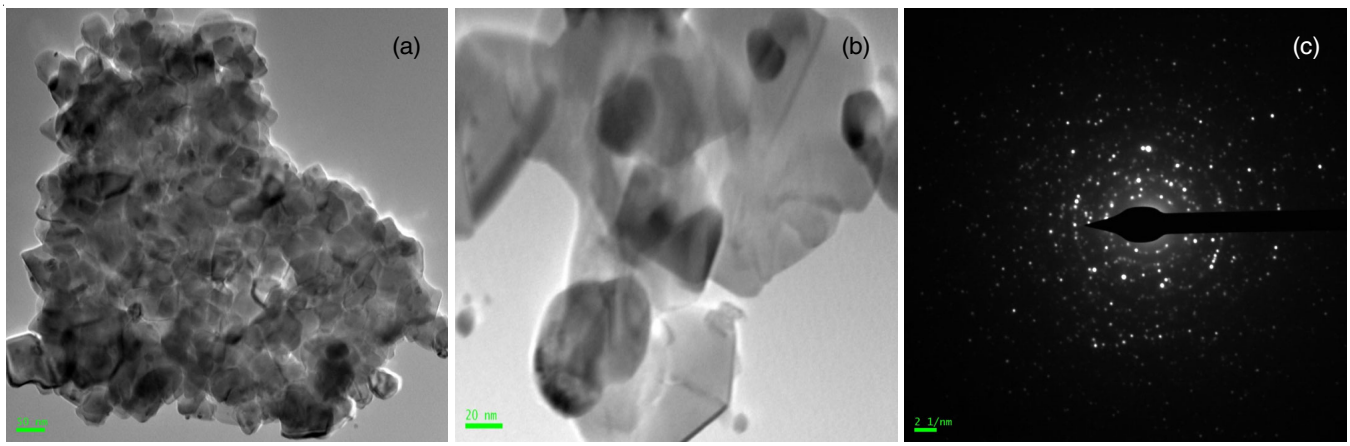

Fig. 2. TEM image of the SM1 nanoparticles with an edge length on the scale of (a) 50 nm, (b) 20 nm and (c) SEAD image of SM1 nano crystalline particles

thin layer of MoS_2 attached in tiny quantities. The SEAD map (Fig. 2c) shows the ring-like electron diffraction patterns, which implies that the crystallinity is consistent with the structure.

SEM micrograph: Fig. 3(a-f) depicts the change in morphology of SM and SM1 samples with uneven size and shape. Different sized nanocrystals were related to the size decrease of particles to the quantum confinement effect of nanoparticles. Agglomeration decreases due to MoS_2 coating.

Significantly smaller uneven spherical and rod-like particles and high agglomeration were observed in sample SM1. From the above SEM images, a denser morphology was observed. The particle size increases with the coating of MoS_2 and a diffused octahedral shape is observed in sample SM1.

EDAX studies: The energy dispersive X-ray analysis (EDAX) of samples SM and SM1 (Fig. 4a-b) confirmed the presence of Ag, Cr, Mo, O and S with appropriate proportions in the related nanoparticles, further proving the formation of a coating. The EDAX spectrum of the SM1 shows a strong Mo and S signal around 2-3 keV, confirming that the external shell is composed of MoS_2. From EDX analysis, the atomic % and weight % were calculated as an exact amount of composition and are compared with theoretically obtained values as shown in Table-2.

Zeta potential: The zeta potential of sample SM1, as shown in Fig. 5a, was obtained, which rationalizes the observed excellent long-term stability of the colloidal suspension. The stability of suspensions can be influenced in a variety of ways. The stability of suspensions can be monitored by measuring the zeta potential. Suspensions of SM1 nanoparticles were stable in the neutral pH range. The mean value of SM nanoparticles

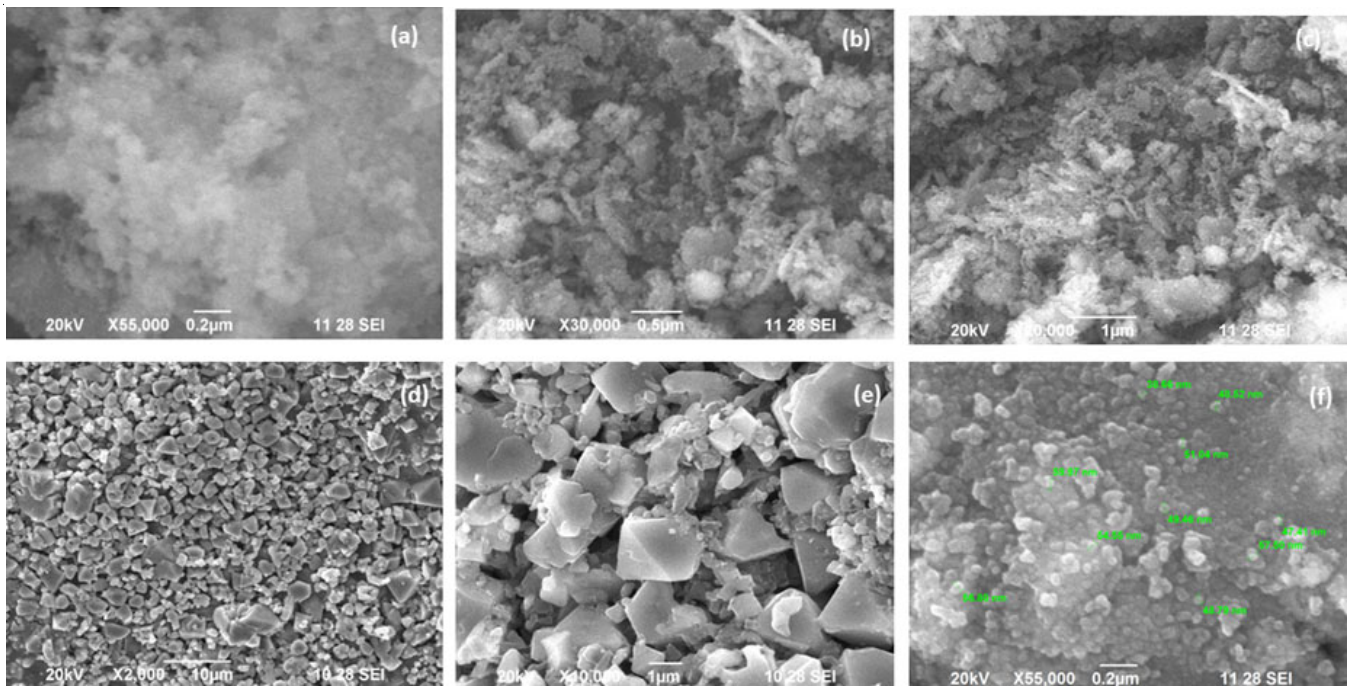

Fig. 3. SEM images at different magnifications (a-c) SM and (d-f) SM1 nanocrystalline particles

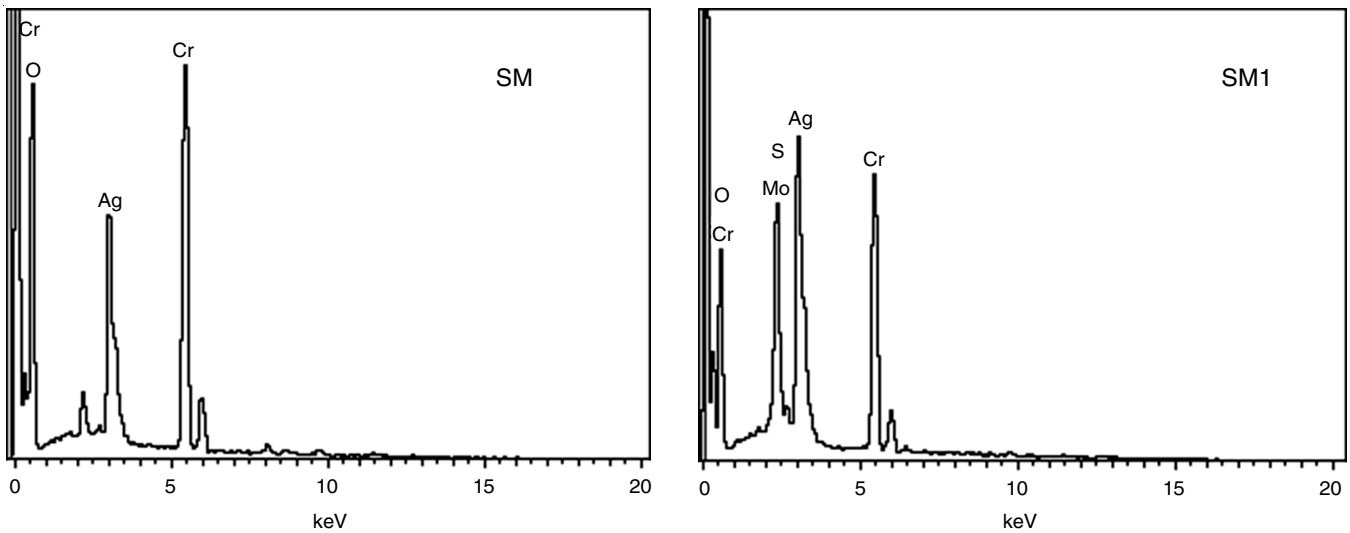

Fig. 4. EDAX spectra of SM and SM1 nanocrystalline particles

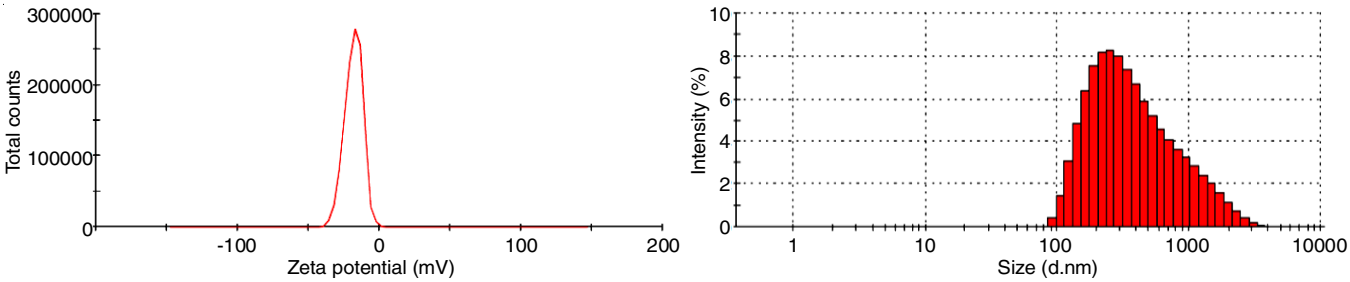

Fig. 5. Zeta potential and particle size distribution of SM1

TABLE-2
ELEMENTAL WEIGHT AND ATOMIC %
OF SM AND SM1 NANOPARTICLES

SM			SM1		
Element	Weight (%)	Atomic (%)	Element	Weight (%)	Atomic (%)
O K	39.68	72.69	O K	36.45	70.51
Cr K	37.39	21.08	S K	5.08	4.91
Ag L	22.93	6.23	Cr K	24.73	14.72
			Mo L	5.22	1.68
			Ag L	28.52	8.18

was found to be -18.2 d.nm, while the average particle size of SM nanoparticles was 291.7 d.nm. The particle size distribution can be affected by a number of factors such as the process of sonification, which involves the addition of a stabilizer [26].

Magnetic properties: Fig. 6 shows the magnetic behaviour of the samples SM and SM1 investigated by a vibrating sample magnetometer (VSM). The formation of a hysteresis loop in the cyclic range indicates ferromagnetic behaviour with coercivity values ~89 G and ~105 G, respectively. The magnetization values of the samples were 0.6943 emu/g and 1.0258 emu/g, respectively. Magnetization value increases due to adding MoS_2 layers to SM nanoparticles, as shown in Table-3.

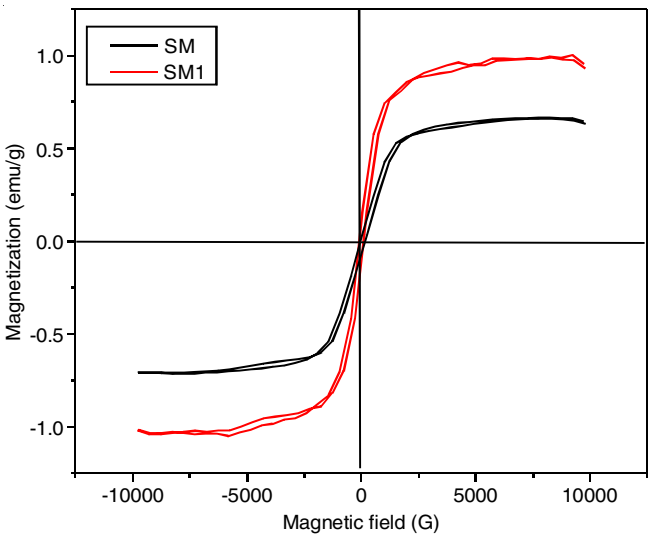

Fig. 6. M-H hysteresis loop of SM1

UV-Vis DRS spectra: It is confirmed that the introduction of ultrathin MoS_2 layers enhances the UV-vis absorption of Ag/Cr_2O_3 (Fig. 7a) implies a better light photoresponse and preferable UV-vis photolight catalytic activity. The optical

TABLE-3
MAGNETIC PROPERTIES OF SM AND SM1

Magnetic properties	SM	SM1
Coercivity (Hci)	88.977 G	106.08 G
Magnetization (Ms)	0.69438 emu/g	1.0258 emu/g
Retentivity (Mr)	84×10^{-3} emu	143×10^{-3} emu
Susceptibility	3.15×10^{-4} ?emu/g	4.65×10^{-4} ?emu/g
Field at Ms	9.7×10^{3} G	9.8×10^{3} G

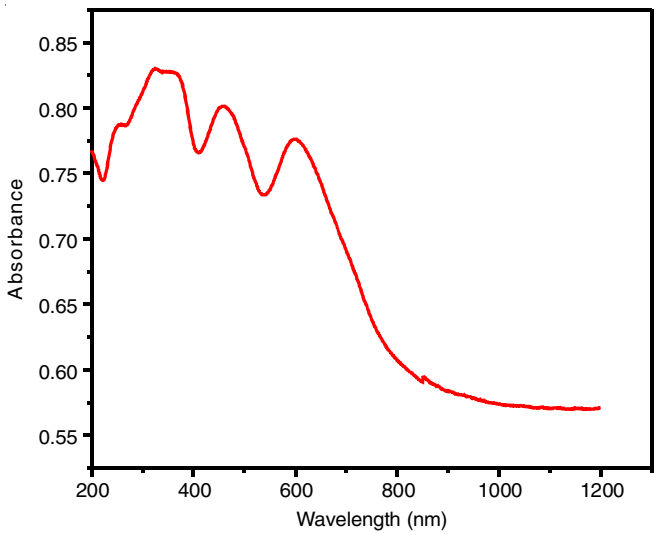

Fig. 7. UV-vis DRS spectrum of SM1

absorption properties of nanoparticles generally exhibit significant changes due to quantum effect, size effect and large surface area. When the nanoparticles were smaller than the wavelength of the light, free electrons might be transferred from the lattice of positive ions in resonance with light. A broad peak located around 340 nm is attributed to the plasmon resonance of Ag nanoparticles [27]. Peaks at 456 nm and 610 nm were the characteristic absorption bands of ultrathin layer MoS_2 arising from the K point of the Brillouin zone were observed. The band gap of Cr_2O_3 and MoS_2 decreases from 3.4 eV and 1.68 eV to 1.06 eV, respectively, due to strong interaction.

The optical indirect band gap values of the sample is determined by Tauc's relation [28]. The plots of hν *versus* $(\alpha h\nu)^{1/2}$ for SM1 sample is shown in Fig. 8. The The estimated indirect band gap value for SM1 is 1.06 eV.

$$\alpha h\nu = A(h\nu - E_g)^n \quad (2)$$

where A, hν, α and E_g are the absorbance, photon energy, constant and optical band gap of the nanoparticles, respectively. The absorption coefficient (α) of the powders at different wave-

lengths can be calculated from the absorption spectra and n = 1/2 for the indirect band gap.

Cytotoxicity studies: The anticancer efficacy of the SM1 nanocomposite was evaluated using the MTT assay against MCF-7 adenocarcinoma and HepG-2 cancer cell lines at five different concentrations (5, 25, 50, 75 and 100 µg/mL) and compared to the normal control. The sample shows anticancer potential in both cell lines and adding SM1 at different doses enhances the percentage of anti-proliferation in MCF-7 (Fig. 9a) and HepG-2 (Fig. 9b) cell lines for 4 h treatment. The % inhibition is proportional to the concentration of nanoparticles [29] (Table-4). Fig. 9 reveals that the reduced cell viability observed at different concentrations of both MCF-7 and HepG-2 cell lines was due to the efficient heat-induced cell killing of SM1 sample. Moreover at low concentrations, the SM1 nanocomposite outperformed HepG-2 cancer cells regarding cytotoxicity. After 4 h of SM1 treatment, the morphology of the MCF-7 and HepG-2 cell lines showed substantial changes in morphology and decreased cell density, indicating apoptotic cells [30]. It is usually assumed that the action of a chemical on cancer cells is primarily due to oxidative stress. Conversely, tumor cells may depend on a precise amount of H_2O_2 and a lack of it might lead to cell cycle arrest or apoptosis.

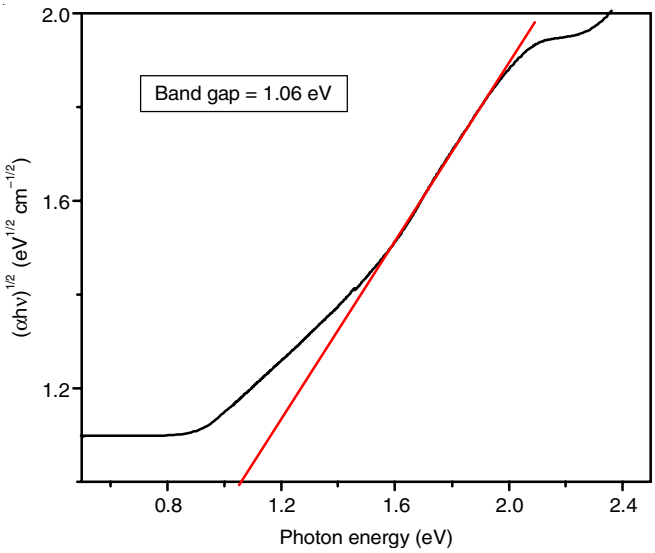

Fig. 8. Band-gap values assessed by a correlated curve of $(\alpha h\nu)^{1/2}$ against photon energy plots of SM1

TABLE-4
PERCENTAGE ANTI-PROLIFERATION OF MCF-7 AND HepG-2 CANCER CELL LINES TREATED WITH SM1 AT DIFFERENT CONCENTRATIONS

Concentration (µg/mL)	Percentage proliferation MCF-7 cell line	Percentage proliferation HepG-2 cell line
5	54	62
25	55	66
50	70	70
75	74	81
100	78	84

Antibacterial activities: The inhibitory zones SM1 of Gram-positive and Gram-negative microbial strains confirmed that the activity was proportional to the material concentration. The growth inhibition improves as the concentration rises to 100 µg/mL. The effect of SM1 nanocomposite on bacterial linear growth revealed that increasing the concentration of the nanocomposite decreased bacterial growth. The study found that SM1 concentration inhibits the growth of both Gram-negative and Gram-positive bacteria. As shown in Table-5, increasing the concentration by 10, 20, 40, 60, 80 and 100 µg/mL increased the zone of inhibition. According to the literature, the percentage of inhibition of *E. coli* was also higher [31].

TABLE-5
ANTIBACTERIAL ACTIVITIES OF SM1

Concentration (µg/mL)	Zone of inhibition (mm)	
	Gram-positive bacterial strain (*S. aureus*)	Gram-negative bacterial strain (*E. coli*)
Positive control	26	20
10	0	2
20	7	5
40	10	6
60	13	7
80	15	10
100	16	12

Conclusion

Facile synthesis of hollow core-shell nanoparticles silver/Cr_2O_3 embedded with ultrathin MoS_2 layers was achieved *via* two steps of sol-gel auto combustion and sonification route. The analysis of the powder XRD pattern of the SM and SM1 samples confirmed its phase purity and structure, respectively. The particle size varies from nanometers to micrometers range which is crystallite sizes were in the nanoscale and good agreement with powder XRD results. EDAX spectra of the samples confirmed the purity of the sample prepared in each stage and agree with the atomic weight percentage shown in the coating of MoS_2 ultrathin layers. From the TEM images, silver nanoparticles were predominantly spherical and visible the silver nanoparticles embedded on Cr_2O_3 and the ultrathin layer of MoS_2 attached. Particle size analysis also supports the average particle size of sample SM nanoparticles. The optical absorbance measurements over the range 200-8120 show the three broad clear peaks were due to the absorbance of the visible and NIR light that gives the conformation of nanosilver particles embedded on Cr_2O_3 and ultrathin MoS_2 layers. Peaks at 456 nm and 610 nm were the characteristic absorption bands of ultrathin layer MoS_2 arising from the K point of the brillouin zone are observed. The band gap of Cr_2O_3 and MoS_2 decreases from 3.4 eV and 1.68 eV to 1.06 eV, respectively, due to the strong interaction. Magnetic studies show that the formation of a hysteresis loop in the cyclic range indicates the ferromagnetic nature at 300 K. Even at low doses, the enhanced percentage of anti-proliferation was attributed to improved biocompatibility of customized SM nanoparticle with MoS_2, which is a good candidate for hyperthermia for a short period. The SM1 nanocomposite displayed potential antibacterial action in Gram-positive and Gram-negative bacterial strains in a dose-dependent manner, indicating that SM1 is a promising candidate for food and biomedical applications.

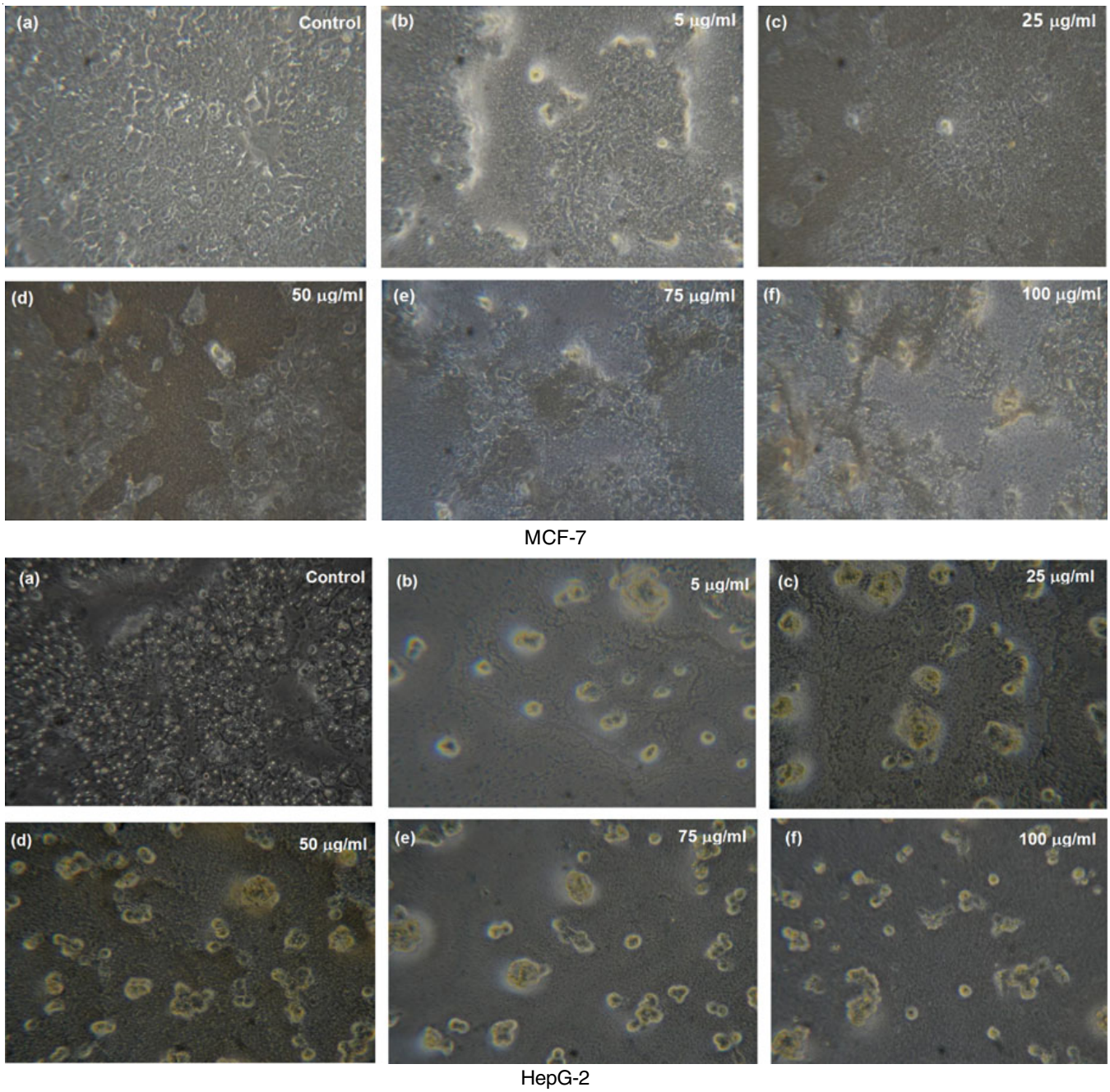

Fig. 9. Cytotoxic assay (MTT) of SM1 on MCF-7 and HepG-2 at different concentrations (a) control (b) 5 µg/mL (c) 25 µg/mL (d) 50 µg/mL (e) 75 µg/mL (f) 100 µg/mL for 4 h

ACKNOWLEDGEMENTS

The authors acknowledge the support of Pondicherry University for XRD, XPS analyses and SITRA, Coimbatore, India for anticancer activity.

CONFLICT OF INTEREST

The authors declare that there is no conflict of interests regarding the publication of this article.

REFERENCES

1. N. Baig, I. Kammakakam and W. Falath, *Mater. Adv.*, **2**, 1821 (2021); https://doi.org/10.1039/D0MA00807A
2. A.A. Yaqoob, H. Ahmad, T. Parveen, A. Ahmad, M. Oves, I.M.I. Ismail, H.A. Qari, K. Umar and M.N. Mohamad Ibrahim, *Front Chem.*, **8**, 341 (2020); https://doi.org/10.3389/fchem.2020.00341
3. Q.A. Pankhurst, N.T.K. Thanh, S.K. Jones and J. Dobson, *J. Phys. D Appl. Phys.*, **42**, 224001 (2009); https://doi.org/10.1088/0022-3727/42/22/224001
4. Y. Zhao, Z. Zhang, Z. Pan and Y. Liu, *Exploration*, **1**, 20210089 (2021); https://doi.org/10.1002/EXP.20210089
5. X. Qiu, Y. Zhang, Y. Zhu, C. Long, L. Su, S. Liu and Z. Tang, *Adv. Mater.*, **33**, 2001731 (2021); https://doi.org/10.1002/adma.202001731
6. S. Bhatnagar, T. Kobori, D. Ganesh, K. Ogawa and H. Aoyagi, *Nanomaterials*, **9**, 1042 (2019); https://doi.org/10.3390/nano9071042

7. Q. Xiong, S. Altnji, T. Tayebi, M. Izadi, A. Hajjar, B. Sundén and L.K.B. Li, *Sustain. Energy Technol. Assess.*, **47**, 101341 (2021); https://doi.org/10.1016/j.seta.2021.101341
8. B.-Y. Song, M. Yang, L.-H. Liu, X.-F. Zhang, Z.-P. Deng, Y.-M. Xu, L.-H. Huo and S. Gao, *Chem. Eng. J.*, **450**, 138211 (2022); https://doi.org/10.1016/j.cej.2022.138211
9. R. Kempt, A. Kuc and T. Heine, *Angew. Chem.*, **59**, 9242 (2020); https://doi.org/10.1002/anie.201914886
10. B.H. Choi, M.R. Kim, Y.N. Jung, S. Kang and J. Hong, *Int. J. Mol. Sci.*, **24**, 562 (2022); https://doi.org/10.3390/ijms24010562
11. J.R. Hood, J.M. Wilkinson and H.M.A. Cavanagh, *J. Essent. Oil Res.*, **15**, 428 (2003); https://doi.org/10.1080/10412905.2003.9698631
12. J. Singh, R. Kumar, V. Verma and R. Kumar, *Mater. Sci. Semicond. Process.*, **123**, 105483 (2021); https://doi.org/10.1016/j.mssp.2020.105483
13. K.C. Lalithambika, K. Shanmugapriya and S. Sriram, *Appl. Phys., A Mater. Sci. Process.*, **125**, 817 (2019); https://doi.org/10.1007/s00339-019-3120-9
14. Z. Liang, R. Shen, Y.H. Ng, P. Zhang, Q. Xiang and X. Li, *J. Mater. Sci. Technol.*, **56**, 89 (2020); https://doi.org/10.1016/j.jmst.2020.04.032
15. Z. Li, H. Li, S. Wang, F. Yang and W. Zhou, *Chem. Eng. J.*, **427**, 131830 (2022); https://doi.org/10.1016/j.cej.2021.131830
16. S.-T. Wan, H.-T. Li, Z.-H. Ma, H.-C. Zhang and Y.-Z. Zheng, *Rare Met.*, **41**, 1735 (2022); https://doi.org/10.1007/s12598-021-01954-3
17. W. Zheng, Y. Xu, L. Zheng, C. Yang, N. Pinna, X. Liu and J. Zhang, *Adv. Funct. Mater.*, **30**, 2000435 (2020); https://doi.org/10.1002/adfm.202000435
18. D. Gupta, V. Chauhan and R. Kumar, *Inorg. Chem. Commun.*, **121**, 108200 (2020); https://doi.org/10.1016/j.inoche.2020.108200
19. O. Samy, S. Zeng, M.D. Birowosuto and A. El Moutaouakil, *Crystals*, **11**, 355 (2021); https://doi.org/10.3390/cryst11040355
20. F. Bussolotti, T.D. Maddumapatabandi and K.E.J. Goh, *Math. Quantum Technol.*, **3**, 032001 (2023); https://doi.org/10.1088/2633-4356/acd907
21. S. Çitoglu, Ö.D. Coskun, L.D. Tung, M.A. Onur and N.T.K. Thanh, *Nanomedicine*, **16**, 925 (2021); https://doi.org/10.2217/nnm-2020-0467
22. P. Joensen, F.R. Frindt and S.R. Morrison, *Mater. Res. Bull.*, **21**, 457 (1986); https://doi.org/10.1016/0025-5408(86)90011-5
23. C. Singh, S.K. Anand, K.N. Tiwari, S.K. Mishra, P. Kakkar, *3 Biotech.*, **11**, 115 (2021); https://doi.org/10.1007/s13205-021-02654-6
24. M.K. Hossain, A.W. Mukhaimer and M. Al-Jabari, *J. Nanopart. Res.*, **23**, 89 (2021); https://doi.org/10.1007/s11051-021-05201-9
25. J. Zhao, G. Liu, Y. Zhang, J. Dong, Y. Wang, Y. Liu, H. Li and J. Xia, *Colloids Surf. A Physicochem. Eng. Asp.*, **648**, 129357 (2022); https://doi.org/10.1016/j.colsurfa.2022.129357
26. G. Arun Kumar, H.S. Bhojya Naik, R. Viswanath, I.K. Suresh Gowda and M. Vinuth, *Mater. Today Proc.*, 43932 (2017); https://doi.org/10.1016/j.matpr.2017.02.293
27. T. Kiba, K. Masui, Y. Inomata, A. Furumoto, M. Kawamura, Y. Abe and K.H. Kim, *Vacuum*, **192**, 110432 (2021); https://doi.org/10.1016/j.vacuum.2021.110432
28. P.R. Jubu, F.K. Yam, V.M. Igba and K.P. Beh, *J. Solid State Chem.*, **290**, 121576 (2020); https://doi.org/10.1016/j.jssc.2020.121576
29. S. Zadaliasghar, E. Rahimpour, M. Khoubnasabjafari, M.H. Pournaghi-Azar, A. Nokhodchi and A. Jouyban, *J. Mol. Liq.*, **316**, 113891 (2020); https://doi.org/10.1016/j.molliq.2020.113891
30. Z.E. Goldblatt, H.A. Cirka and K.L. Billiar, *Ann. Biomed. Eng.*, **49**, 75 (2021); https://doi.org/10.1007/s10439-020-02659-x
31. T.T.T. Vi, S.R. Kumar, J.H.S. Pang, Y.K. Liu, D.W. Chen and S.J. Lue, *Nanomaterials*, **10**, 366 (2020); https://doi.org/10.3390/nano10020366